ESTIMATION OF SURFACE FAULT DISPLACEMENT BY HIGH PERFORMANCE COMPUTING

Muneo Hori[*], Masataka Sawada[†], and Kazumoto Haba[‡]

Abstract

For more reliable estimation of the occurrence and displacement of surface earthquake fault, we develop a high-performance-computing finite-element-method (HPC-FEM), to which a scalable solver based on a conjugate gradient method is implemented. HPC-FEM is aimed at solving an initial boundary value problem of fault rupture process. The solution of this problem is mathematically unstable, and we enhance HPC-FEM with the following two features: 1) a symplectic time integration of an explicit scheme for proper conservation of energy; and 2) a rigorously formulated joint element of high order. The verification of HPC-FEM is made by comparing the results of quasi-analytical solutions. It is shown that HPC-FEM is able to compute the critical base slip that makes the rupture reach the ground surface. The accuracy and reliability of the estimation of fault displacement are sexamined by making numerical experiments, and the utilization of HPC-FEM for the rupture process simulation is discussed.

Keywords: Surface earthquake fault, high performance computing, finite element method, symplectic time integration, joint element

1 Introduction

For the safety of nuclear power plants, it is necessary to estimate a possibility of the occurrence and the amount of displacement for a surface earthquake fault; see Fig. 1. A fundamental mechanism of the surface earthquake fault is the rupture propagation on the fault plane that is confined by the surrounding rock. If sufficiently large rupture takes place, the fault appears on the ground and fault displacement is induced. While studying a scenario of the slip on the fault plane is an issue of seismology, the following problem could be a target of rock mechanics:

> the rupture process on a shallow part of a fault plane that is constrained by rock mass, when a slip is prescribed at the bottom of the shallow part.

This problem can be formulated as a continuum mechanics problem for rock mass in which plane of displacement discontinuity is embedded.

Numerical simulation of the fault rupture processes is a method of solving the above posed problem. Indeed, in practice, the following two-step simulation is conducted[11]: 1) evaluating the boundary displacement of an area in view of the crust deformation that is based on the elastic theory of dislocation[14]; and 2) evaluating the deformation of the target area by analyzing a detailed model of higher resolution and fidelity. However, the rupture process simulation that is used to estimate surface earthquake fault is limited[4]. The rupture simulation, which uses finite difference method (FDM), boundary element method (BEM) or finite element method (FEM)[1, 10, 12, 13], is used mainly to evaluate strong ground motion.

In the mechanical viewpoint, a fundamental difficulty in analyzing the fault rupture process is the need of a large scale model of high spatial resolution. A large amount of numerical computation is needed. Also, we have to point out the loss of stability of the mathematical solution of the fault rupture process. The stability implies that a solution does

[*]Corresponding author, Earthquake Research Institute, The University of Tokyo, 1-1-1 Yayoi Bunkyo-ku, Tokyo, 113-0032, Japan
[†]Nuclear Risk Research Center, Central Research Institute of Electric Power Industry, 1646 Abiko, Abiko, 270-1194, Japan
[‡]Nuclear Facilities Division, Taisei Corporation, 1-25-1 Nishi-shinjuku Shinjuku-ku, Tokyo, 163-0606, Japan

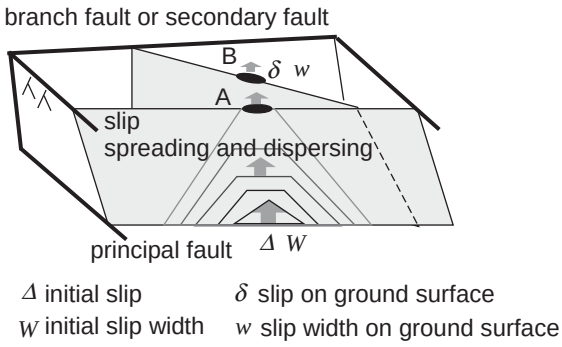

Figure 1: Spreading and dispersing of a slip on faults

not change when small disturbance is given to problem setting, and the stability loss means that a significant change is induced in the solution when small disturbance is given; see Fig. 2. The mathematical stability loss inherently induces the loss of stability in numerical computation.

The numerical analysis of the fault rupture process needs a most advanced numerical analysis method, with which the numerically convergence is guaranteed for a mathematically unstable solution. The utilization of high performance computing (HPC) is inevitable to carry out a large scale numerical analysis. Capability computing, which solves an analysis model of a largest degree-of-freedom (DOF) in a shortest time increment, is needed to this end. Beside for a possible rupture scenario, the fault plane and the rock mass have numerous uncertainties in the configuration and material properties. Capacity computing, which carries out the analysis of many models and initial/boundary conditions just like Monte-Carlo simulation, is needed to quantify the effects of such uncertainties on the estimation of surface earthquake fault.

In this paper, we present HPC-FEM, an FEM program enhanced with HPC capability, to numerically analyze the fault rupture process for the estimation of surface earthquake fault, This HPC-FEM implements a *solver*, a module of solving a matrix equation, which is based on a conjugate gradient method, and high scalability is guaranteed. The contents of the present paper as follows: In the study, we first review the mechanism of fault rupture processes and clarify the need for accurate numerical analysis of the process. We present an explicit symplectic integration for the time integration and joint element which is rigorously formulated. Numerical experiments of solving the fault rupture process using HPC-FEM are made to verify the program. The utilization of HPC-FEM for the estimation of surface earthquake fault is discussed, based on the results of the numerical experiment.

2 Stablity of Fault Rupture Process

A simple schematic diagram is presented in Fig. 2 to explain the loss of the mathematical stability for the fault rupture process. This diagram shows the relation between the slip and the traction. We first consider controlling the slip. As we increase the slip, the traction increases. Once it reaches the critical value, the traction starts to decrease as we increase the slip.

We next consider controlling the traction. As we increase the traction, the slip increases. Once the traction reaches the critical value, we have to decrease the traction to increase the slip. However, on the descending part, keeping the traction constant is not easy, because the traction tends to decrease together with the increase in the slip. Indeed, for a small perturbation to the traction, the slip changes on the descending part; the slip does not change on the ascending part unlike the descending part. This behavior of the slip on the descending part is the loss of the stability.

A stable solution corresponds to a process that needs external work to increase its internal energy. On the descending part, the work done is converted to the friction energy. A process that releases the internal energy to the external work is regarded as an unstable solution, because this process automatically continues until sufficient internal energy is released.

More rigorous explanation can be made by using the wave equation. The loss of stability occurs when the natural frequency of the wave equation changes from a real number to an imaginary number (or a temporally sinusoidal

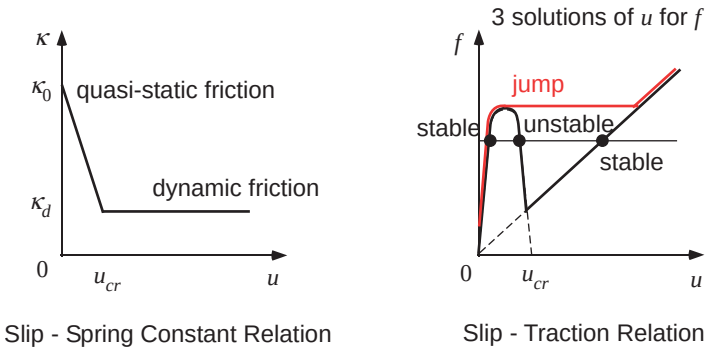

Figure 2: Friction characteristics and slip–traction relation

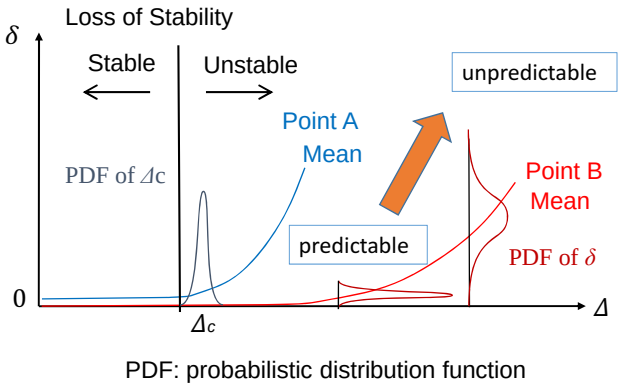

Figure 3: Prediction of the surface fault displacement

response changes to a temporally exponential response). As for the fault rupture process, this change is caused by the friction characteristics of the fault plane. If the slope between the slip-traction relation is positive, the natural frequency is a real number. However, the slop becomes negative, it becomes an imaginary number.

It should be mentioned that there exists a unique solution for the fault rupture process. The stability of this solution is lost when the characteristic of the fault surface friction changes. To compute this solution, we need HPC since the target area is of the order of 10^3 m. The time resolution is of the order of 10^{-2}, which results in the spatial resolution of 10^1 m for the wave velocity of 10^3 m/s.

It is important to note the treatment of uncertainty due to the limitation in the quality and quantity of relevant data which are available for the underground structure, stress state, and source fault dynamics that determines the input slip for the shallow part. We can take advantage of capacity (or ensemble) computing of HPC to evaluate the variability in the occurrence and displacement of the surface earthquake fault that is induced by the uncertainty; see Fig. 3.

When high uncertainty exists, displacement of surface earthquake fault, denoted by δ, are distributed in a wider range for a given input slip, denoted by Δ. In this case, δ might be regarded as unpredictable in practice. It is considered as important to evaluate the critical input slip, Δ_c, that makes the rupture reach the ground surface, prior to evaluating δ.

3 Key Features of HPC-FEM

To accurately compute an unstable solution of the fault rupture problem, we enhance HPC-FEM with the following two features; 1) a joint element that rigorously accounts for displacement discontinuity; and 2) a modern symplectic time integration for energy conservation.

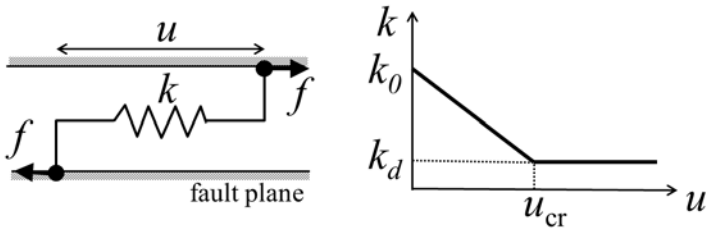

Figure 4: Simple spring model.

3.1 Symplectic time integration

Symplectic integration is designed to solve canonical equation of Hamiltonian[9, 15, 19]. A widely used class of symplectic integration are formulated by using the splitting method which is used for a Hamiltonian $\mathcal{H}$ of the following form:

$$\mathcal{H}(u, p) = \mathcal{T}(p) + \mathcal{V}(u). \tag{1}$$

Here, p and q are (generalized) momentum and displacement, respectively, and T and V are kinetic and potential energy, respectively. The canonical equations are expressed in terms of p and q as follows:

$$\frac{\mathrm{d}u}{\mathrm{d}t} = \frac{\mathrm{d}\mathcal{T}}{\mathrm{d}p} \quad \text{and} \quad \frac{\mathrm{d}p}{\mathrm{d}t} = -\frac{\mathrm{d}\mathcal{V}}{\mathrm{d}u}. \tag{2}$$

The symplectic time integration of the first-order is formulated, as

$$\begin{cases} u_{n+1} &= u_n + \Delta t \nabla_p \mathcal{T}(p_n), \\ p_{n+1} &= p_n - \Delta t \nabla_u \mathcal{V}(u_{n+1}), \end{cases} \tag{3}$$

where Δt is a time increment, and subsript n indictes the value of n-th time step. Thus, u_{n+1} and p_{n+1} are computed explicitly. Symplectic integrations of higher orders are formulated in a similar manner.

We examine the efficiency of the symplectic time integration, compared to the Newmark β method[17], which is a standard implicit time integration method. We solve a simple spring model subjected to external force f; see Fig. 4. The spring constant exhibits nonlinearity similar to that shown in Fig. 2. The canonical equation is derived as follows:

$$\frac{\mathrm{d}u}{\mathrm{d}t} = \frac{p}{m} \quad \text{and} \quad \frac{\mathrm{d}p}{\mathrm{d}t} = -2k_0 u + 2C_k u^2 + 2f,$$

where u and p are the relative displacement and the relative momentum, respectively; m is the mass, k_0, k_d and u_{cr} are the initial spring constant, the final spring constant, and the critical relative displacement; and $C_k (= k_0 - k_d)/u_{cr}$ is the reduction rate of the spring constant. The values of these parameters are set as $m = 1.0\,\mathrm{kg}$, $f = 0.4\,\mathrm{N}$, $k_0 = 0.75\,\mathrm{N/m}$, $C_k = 0.25\,\mathrm{N/m^2}$.

In Fig. 5, we plot the time series of the relative displacement; u and t are normalized by using $u_{\max} = 1.737652\,\mathrm{m}$ and the elapsed time $\bar{T} = 8.265\,\mathrm{s}$, where $u_{\max}$ is the maximum value of the relative displacement, i.e.,

$$u_{\max} = \frac{3k_0}{4C_k}\left(1 - \sqrt{1 - \frac{16}{3}\frac{TC_k}{k_0^2}}\right). \tag{4}$$

An accurate solution of Eq. (4) is computed by using *Mathematica*; the accuracy and precision are set infinity.

The Newmark-β method is used as an alternative of the symplectic time integration; the parameters are set as $\beta = 0.25$ and $\gamma = 0.5$. We adopt a second-order symplectic integration such that the order of convergence is the same as that of the Newmark-β method. Used are time increment of 1/10, 1/20, 1/50, 1/100, 1/200, 1/500, and 1/1000 of $\bar{T}$. Figure 5 shows the time series of the relative displacement for $\Delta t = 1/1000$, 1/100, and 1/10 of $\bar{T}$. In both the

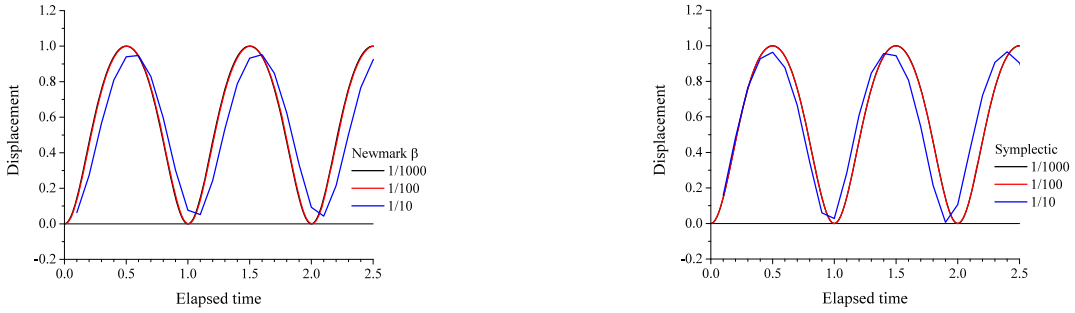

a) Newmark β b) symplectic

Figure 5: Progression of the relative displacement

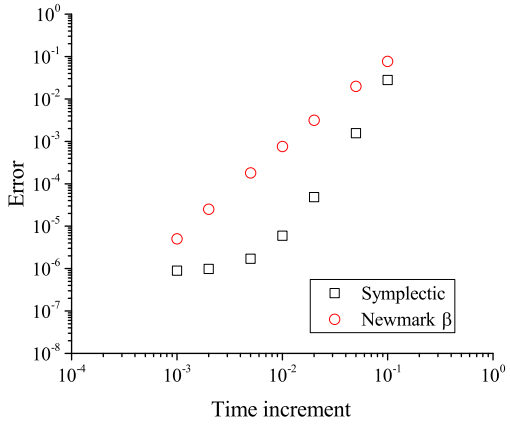

Figure 6: Evaluation of error

Newmark-β method and the symplectic integration, the amplitude and phase are accurately computed except for the case of $\Delta t = 1/10\,\bar{T}$.

Figure. 6 shows the relationship between the error of the solution and the time increment. Here, the error is defined as the relative difference between the computed solution and the *Mathematica* solution after one period. Second-order convergence is observed for the Newmark-β method. The error and the convergence rate of the symplectic integration are smaller and faster, respectively, compared with those of the Newmark-β method.

3.2 Nonlinear Spring Model on Fault

In joint elements which are used in rock mechanics, nodal force is calculated from the difference in nodal displacement by using relation between displacement gap and force on a discontinuity[8]. In such joint elements, an element stiffness matrix is easily calculated. However, on the rigorous mechanical viewpoint, questioned is the correctness of computing the nodal force from the nodal displacement. A point-wise displacement gap produces point-wise traction on a plane of discontinuity, and the surface integration of the point-wise traction is converted to nodal force. An element stiffness matrix which is computed in this manner is more complicated.

A joint element which is computed in the above rigorous manner is implemented in HPC-FEM, in order to ensure proper convergence of numerical solution. Formulation of this joint element is readily made by using a Lagrangian of continuum which has a plane of discontinuity; using isoparametric formulation for the surface integration, we can form an element stiffness matrix relatively easily[17, 18].

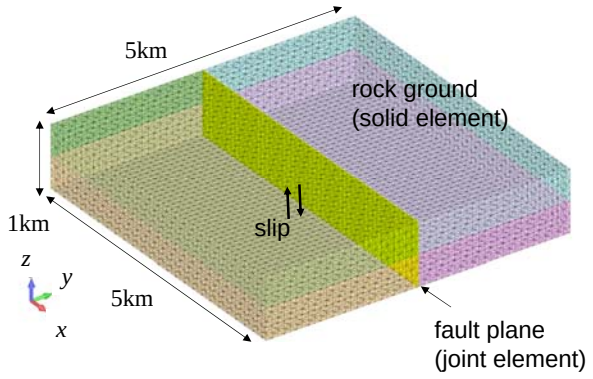

Figure 7: Model for the test simulation 1.

We implement the above joint element with a nonlinear spring model into HPC-FEM. The spring constant per unit area (shear stiffness), denoted by κ, is formulated as a function of displacement gap, denoted by u, as follows:

$$\kappa(u) = \begin{cases} \kappa_0 - \frac{\kappa_0 - \kappa_d}{u_{cr}} u & (u \le u_{cr}) \\ \kappa_d & (u > u_{cr}) \end{cases} \tag{5}$$

where κ_0 and κ_d are the quasi-static and dynamic shear stiffness (the initial or final shear stiffness), respectively, and u_{cr} is the critical slip; see Fig. 2. In the numerical simulations, the trajectory of slip, $u_{traj} = \int \sqrt{\dot{u}_i \dot{u}_i} \mathrm{d}t$ is used for u, where $\dot{u}_i$ is the i-th component of the slip velocity in a Cartesian coordinate system. No sliders or dashpots are used in κ.

An effect of the normal stress on the shear stiffness of faults is accounted; larger normal stress leads to larger shear stiffness. The quasi-static shear stiffness is given as

$$\kappa_0 = a\sigma_n + b, \tag{6}$$

where σ_n is the normal stress on the fault plane, and a and b are constants which correspond to friction and cohesion, respectively.

It should be noted that there is difference in the numerical accuracy of computing displacement and traction for solid element; traction is computed from the spatial derivative of displacement, and hence the accuracy of traction is lower than displacement. In the present joint element, the accuracy of displacement gap and traction is the same since common basis functions are used to discretize them. The mismatch in the accuracy of the joint element and the solid element might result in the loss of the accuracy of a hybrid model which includes joint elements in solid elements.

4 Trial Simulation of Fault Rupture Process

We implemented simplistic time integration and a rigorous joint element into an open-source parallel FEM program, FrontISTR[6]. This program is called HPC-FEM[18].

4.1 Single fault

Frist, using HPC-FEM, we study a single fault in a rock mass. The dimension of an analysis domain is $5 \times 5 \times 1$ km, and a vertical fault plane is embedded; see. Fig. 7 for the analysis model. The model consists of around 1,000 second-order triangle elements for the fault and around 150,000 second-order tetrahedral elements for the rock mass, and has 216,342 nodes and 649,026 DOF.

The input slip, Δ, is applied on the central part of the fault bottom end. A simple symmetric triangle distribution with the width 2.5 km is assumed for the slip, and the maximum slip is 2 m at the midpoint, i.e., one side of the fault is displaced 1 m upwards and the other side 1 m downwards; see Fig. 8). The slip rate at the midpoint is 1 m/s. The side boundaries of the model are set as traction free.

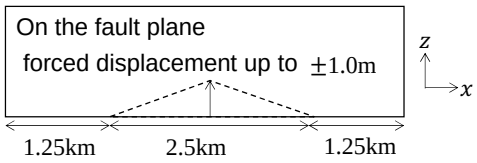

Figure 8: Slip distribution forcibly applied on the bottom of the fault.

Table 1: Material parameters for test simulation.

	Property (unit)	Symbol	Value
Rock	Young's modulus (MPa)	E	1.0×10^4
	Poisson's ratio	ν	0.3
	Density (kg/m^3)	ρ	2.0×10^3
Fault	Quasi-static shear stiffness (MPa/m)	κ_0	1.5×10^2
	Dynamic shear stiffness (MPa/m)	κ_d	(1) $\kappa_0/20$, (2) $\kappa_0/1000$
	Critical slip (m)	u_{cr}	0.1

Table 1 summarizes the material parameters. The rock mass is linear elastic. The fault has static and dynamic shear stiffness of κ_0 and $\kappa_d = 1/20\,\kappa_0$ (Case 1) or $1/1,000\,\kappa_0$ (Case 2). The dependency of the shear stiffness on confining is neglected. It should be noted that a stable solution can be found more easily for Case 1, which is used to verify the developed program, even though Case 2 is more realistic. The value of κ_0 and $1/1,000 = \kappa_d/\kappa_0$ are determined by considering the rock and fault at depths ranging from 0 to 1 km. Figure 9 shows the slip-traction relation for this setting. In Case 2, the traction is hardly recovered, until the slip becomes extremely large.

Figure 10 is the contour of the slip distribution at $t = 2$ s and $t = 3$ s on the fault plane. In Case 1, the slip does not propagate until $t = 2$ s. In Case 2, the slip propagates and reaches the ground surface, and the maximum value of the surface displacement is around 0.6 m.

Figure 11 shows the time series of the slip at three depths along the fault center line. The propagation velocity of the slip is approximately 0.3 km/s from the elevation level (E.L.) -1000 m to E.L. -500 m, and 1 km/s from E.L. -500 m to E.L. 0 m. The observed propagation velocity is 70% of the shear wave velocity[2, 7]. Since the shear wave velocity of the analysis model is 1.5 km/s, the computed propagation velocity is relatively slower than the observed one. This is probably due to higher friction effects. Further investigation is needed to clarify the dependency of the slip propagation velocity on the dynamic shear stiffness.

4.2 Multi-faults

We consider the case where two faults are embedded in the analysis domain considered in the preceding subsection. The fault located at lower or higher depth is regarded as a primary or secondary fault, respectively. The two faults have parallel strikes and opposite dip angles of 40 deg to each other. Figure. 12 presents the analysis model of this multi-faults. The analysis model consists of 7,800 second-order triangle elements for the fault and 157,375 second-order tetrahedral elements for the rock mass, and has 237,435 nodes and 699,750 DOF.

The primary fault is set as a reverse fault. The footwall is set on one side of the primary fault, and has its bottom fixed see Fig. 13a). The slip shown in Fig. 13b) is applied to the central part of the fault bottom edge with the width 1.25 km for the hanging wall side. The slip is also partially applied to the bottom of the hanging wall as shown in Fig. 13a) and c). The maximum value of the input slip and the input slip rate are is 3.1 m and 1.55 m/s, respectively (the duration of inputting slip at the bottom is 2 s). The other outer boundaries are set as traction free. It should be pointed out that an initial distribution of stress is computed by overburdening the weight of the rock mass prior to inputting the slip, and that the effect of normal stress on shear stiffness is taken into consideration.

Table 2 summarizes the material parameters. Although most parameters are the same as those in Table 1, κ_d is

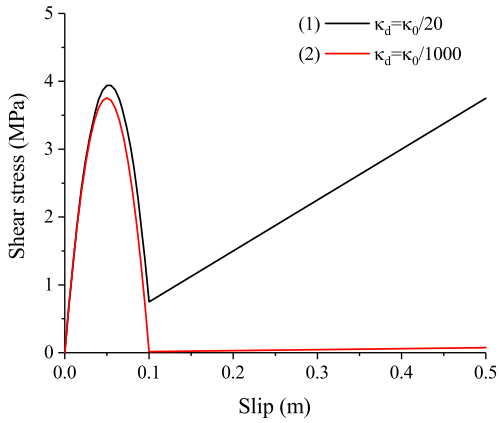

Figure 9: Slip-traction relation on the fault in the test problem.

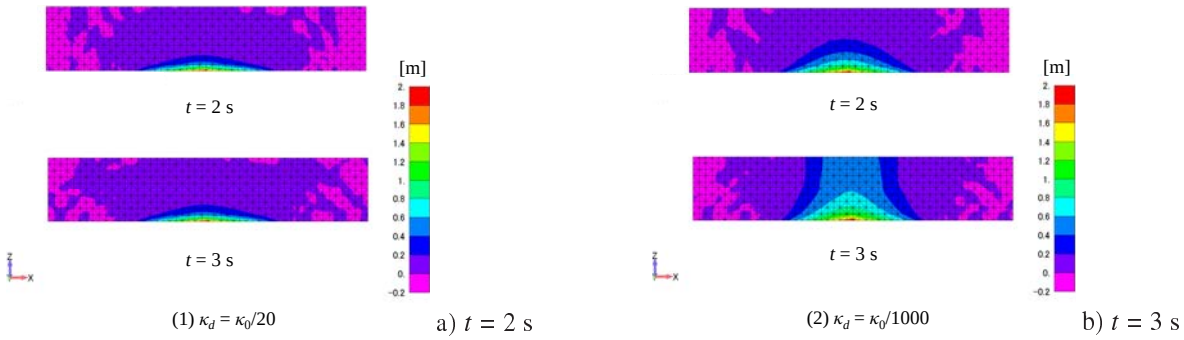

Figure 10: Slip distribution on the fault.

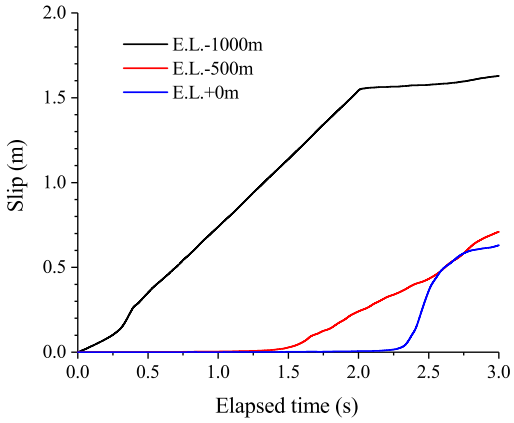

Figure 11: Slip progression at three depths ($\kappa_d = \kappa_0/1000$).

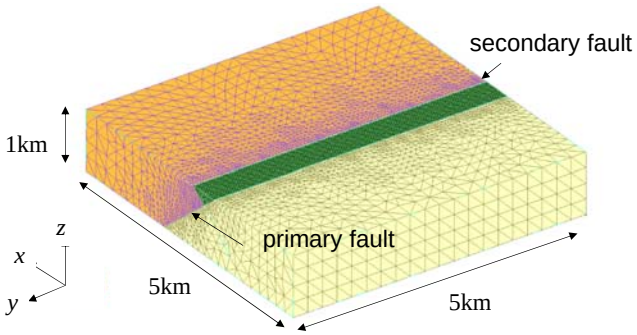

Figure 12: Model for test simulation 2.

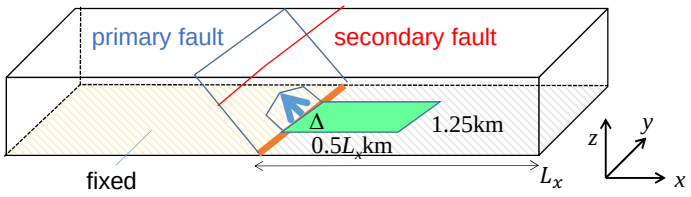

a) Boundary conditions

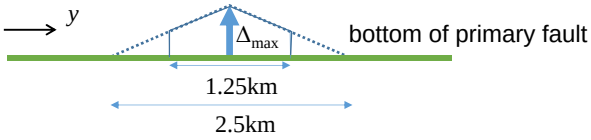

b) Bottom of the primary fault

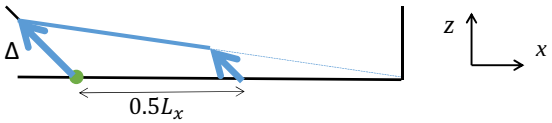

c) On the plane of y=0

Figure 13: Boundary conditions: a) shows boundary conditions, b) shows slip distribution forcibly applied on the bottom of the fault, and c) shows displacement forcibly applied on the plane of $y = 0$.

Table 2: Material parameters for test two.

	Property (unit)	Symbol	Value
Rock	Young's modulus (MPa)	E	1.0×10^4
	Poisson's ratio	ν	0.3
	Density (kg/m^3)	ρ	2.0×10^3
Fault	Quasi-static shear stiffness (MPa/m)	κ_0	(1) 1.5×10^2, (2) $18.5\sigma_n + 0.99$
	Dynamic shear stiffness (MPa/m)	κ_d	$\kappa_0/100$
	Critical slip (m)	u_{cr}	0.1

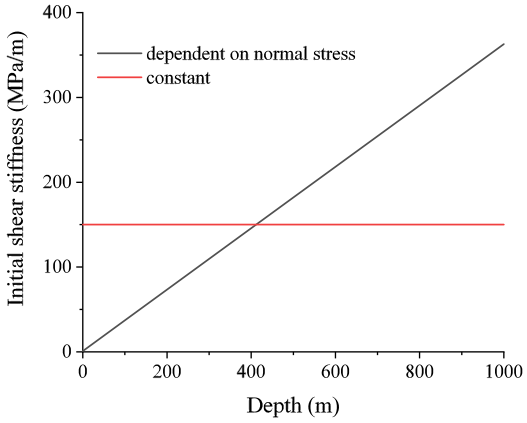

Figure 14: Relation between depth and quasi-static shear stiffness κ_0. Normal stress was assumed as equal to the overburden pressure of ground. The unit of σ_n is MPa.

set as $1/100\,\kappa_0$. Considering the depth-dependent shear stiffness, we use Eq. (6) to define κ_0, with $a = 18.5$ m^{-1} and $b = 0.99$ MPa/m; the values of a and b are chosen such that the first peak of traction in the slip-traction relation (which is similar to Fig. 9) satisfies the Coulomb friction law of $\tau = 0.025 + \sigma_n \tan 25^\circ$ MPa, where τ and σ_n are shear and normal stress. Figure 14 shows the relation between the depth and the static shear stiffness, κ_0, where the normal stress is assumed equal to the overburden pressure of the ground. It should be noted that the shear stiffness of 1.5×10^2 MPa/m corresponds to the median value at depths ranging from -1,000 m to 0 m.

Three damping conditions, namely, no damping and damping factors of 3% and 5% in the Rayleigh damping, are used. It is not possible to set the damping in the simplistic time integration, and the Newmark β method (β=0.25 and $\gamma = 0.5$) is used for the time integration in the cases of damping. Figure 15 shows the time series of slip at the midpoint on the surface and E.L. -500 m of the primary fault; the cases with no damping and 3% damping are plotted, together with the input slip at the midpoint on the bottom edge. The slip reaches E.L. -500 m at 1 s, and it grows vibrating in the period of around 2 s. The vibration tends to be ceased in the case of 3% damping. The slip reaches the surface at 3 s for the case with no damping while it does not reach for the case of 3% damping.

Quasi-static analysis is conducted to approximately evaluate the input slip at the bottom edge that induces the slip on the surface. Figure 16 plots the surface slip with respect to the input slip. As for the comparison, plotted is the slip on the surface computed by the dynamic simulation with 3% and 5% damping; the maximum value of the slip within 3 s is used. The surface slip is almost identical for the quasi-static analysis and the dynamic analysis. It is shown that although the quasi-static analysis is an approximation, it can provide a critical value of the input slip at which slip reaches the surface.

In general, friction characteristic on a fault plane changes depending on confining pressure. Thus, it is taken for

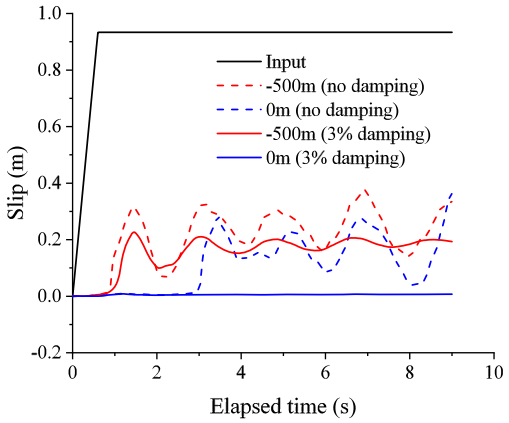

Figure 15: Effect of damping on slip progression.

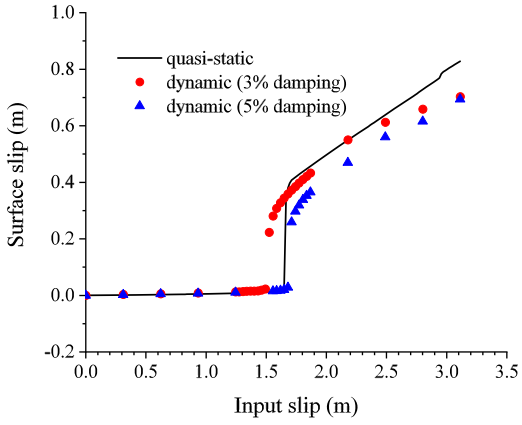

Figure 16: Relationship between input slip and surface slip.

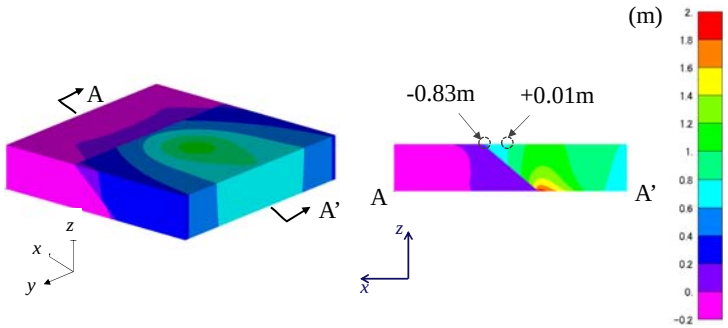

Figure 17: Vertical displacement contour maps in the condition of constant initial shear stiffness at Δ_{max} = 3.1 m.

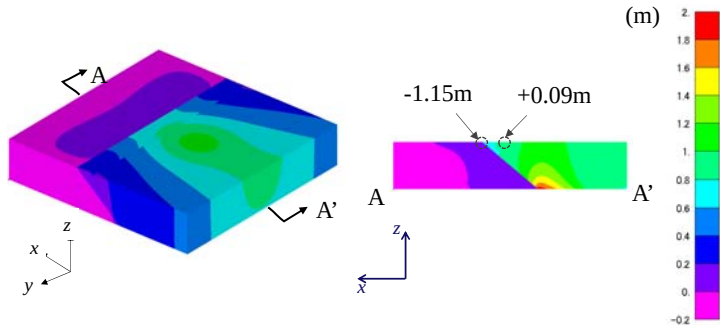

Figure 18: Vertical displacement contour maps in the condition of depth-dependent initial shear stiffness at Δ_{max} = 3.1 m.

granted that the initial shear stiffness, κ_0, increases at a deeper part of the fault plane. Figure 17 shows the contour maps of vertical displacement for the case of constant κ_0. The surface slip at the midpoint of the primary and secondary faults are in the opposite directions, although the amplitude of the secondary fault slip is much smaller. The surface slip of the depth-independent κ_0 is larger than that of the depth-dependent κ_0, because the fault slips more easily in the shallower zone. It is seen that the ground between the primary and secondary faults is lifted (back-thrust like slip), which was observed in the 2014 Nagano-ken-hokubu Earthquake, Japan[3].

5 Usage of HPC-FEM for Surface Earthquake Fault Estimation

The trial simulation of the fault rupture process presented in the preceding section shows at least potential benefit of using HPC-FEM high-performance computing to solve a fault rupture problem by analyzing a large-scale analysis model of high spatial resolution. The solution of the problem loses its stability when the friction changes from the static state to the dynamic state, and HPC-FEM is able to compute the unstable solution. More extensive studies are surely needed to examine the numerical convergence so that the computed solution is close to the exact solution within a certain numerical error.

On the viewpoint of continuum mechanics, the fault rupture process is governed by a wave equation with a non-linear interface that corresponds to a fault plane. The interface behavior is friction, and it is necessary to evaluate friction at all the points on the interface by considering effects of confining pressure that is provided by the deformation of the surrounding rock mass. Hence, it is necessary to use HPC-FEM in order to solve this four-dimensional partial differential equation by analyzing a large scale model.

In the fault rupture process simulation, there are various uncertainties, such as the initial stress distribution, material heterogeneities that include friction characteristics on fault surface, and configuration of rock mass layers. Capacity computing is needed to evaluate the effects of these uncertainties upon the fault rupture process. Capability computing

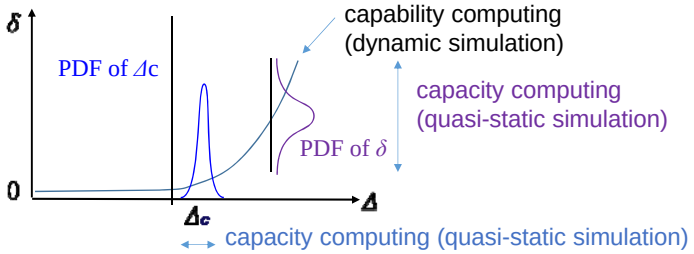

Figure 19: Application of HPC to estimate the surface fault displacement

that uses HPC-FEM will be a useful tool for this evaluation, since it is scalable.

An approximate quasi-static simulation would be of practical importance, since it can provide an estimation of the input slip that makes the slip reach the ground. The input slip is influenced by many factors; most significant factors are the distribution of the input slip at the bottom of the analysis model and the boundary conditions at the bottom surface. The quasi-static simulation is used to select a suitable range for the uncertainties; see Fig. 19).

6 Concluding Remarks

Reliable estimation of surface earthquake fault is crucial to the safety of nuclear power plant facilities. In this study, we develop a finite element method enhanced with high performance computing and implement the following two features:1) a symplectic time integration of explicit scheme to properly conserve the energy of the fault; and 2) igorously formulated joint elements of high order. These two features are essential to compute a mathematically unstable solution of the fault rupture problem.

We made trial numerical simulations of fault rupture process using HPC-FEM. A three-dimensional analysis model of rock mass which includes fault plane is analyzed. It is shown that HPC-FEM is able to obtain an unstable solution, since the analysis model is of sufficiently high spatial resolution. The effect of shear stiffness of fault (that corresponds to static and dynamic friction) on the fault rupture process is studied,

More extensive studies are being made for the utilization of HPC-FEM for the fault rupture problem. A target of primary importance is uncertaintiy quantification, since many uncertain factors such as stress state, material properties, and geological layer configuration as well as input slip, are involved in the fault rupture process. Capacity computing is needed to investigate the effects of these uncertainties upon the fault rupture process.

Acknowledgements

The study is supported by commissioned projects from the Agency for Natural Resources and Energy, Ministry of Economy, Trade and Industry, Japan.

A Hamiltonian of Continuum

Lagrangian is often used to formulate FEM. In this appendix, we derive Hamiltonian for continuum from Lagrangian. We commence from the case where a Lagrangian density, denoted by ℓ, is given to a continuum, V. This ℓ is a function of velocity vector and strain tensor, denoted by $\boldsymbol{v}$ and $\boldsymbol{\epsilon}$, respectively; $\boldsymbol{v}$ and $\boldsymbol{\epsilon}$ are expressed in terms of displacement vector, denoted by $\boldsymbol{u}$, as

$$\boldsymbol{v}(\boldsymbol{x},t) = \dot{\boldsymbol{u}}(\boldsymbol{x},t) \quad \textit{and} \quad \boldsymbol{\epsilon}(\boldsymbol{x},t) = \mathrm{sym}\{\boldsymbol{\nabla u}(\boldsymbol{x},t)\},$$

where $\dot{(.)}$ and $\boldsymbol{\nabla}(.)$ are the temporal derivative and the spatial graident of (.), respectively, and sym stands for the symmetric part of the second-order tensor. A Lagrangian is defined as the volume integral of ℓ.

A Hamiltonian density, denoted by h, is readily derived from a Lagrangian density. Since a Lagrage equation of the Lagrangian density is

$$\frac{\partial}{\partial t}\frac{\partial \ell}{\partial \boldsymbol{v}} + \boldsymbol{\nabla}\cdot\frac{\partial \ell}{\partial \boldsymbol{\epsilon}} = \boldsymbol{0},$$

applying the Legendre transform, $\boldsymbol{p} = \frac{\partial \ell}{\partial \boldsymbol{v}}$, we have

$$h(\boldsymbol{p}, \boldsymbol{\epsilon}) = \boldsymbol{p}\cdot\boldsymbol{v} - (\boldsymbol{v}, \boldsymbol{\epsilon}),$$

where $\boldsymbol{v}$ is regarded as a function of $\boldsymbol{p}$. The cannonical equations of this h are derived from the Lagrange equation and the consistency condition of $\dot{\boldsymbol{\epsilon}} = \mathrm{sym}\{\boldsymbol{\nabla v}\}$, as

$$\dot{\boldsymbol{p}} = \boldsymbol{\nabla}\cdot\frac{\partial h}{\partial \boldsymbol{\epsilon}} \quad \text{and} \quad \dot{\boldsymbol{\epsilon}} = \mathrm{sym}\left\{\boldsymbol{\nabla}\frac{\partial h}{\partial \boldsymbol{p}}\right\}.$$

In formulating FEM in terms of Hamiltonian, we use a discretized displacement function, as follows:

$$\boldsymbol{u}(\boldsymbol{x}, t) = \sum \boldsymbol{u}^{\alpha}(t)\,\boldsymbol{\xi}^{\alpha}(\boldsymbol{x}).$$

Here, $\boldsymbol{u}^{\alpha}$ and $\boldsymbol{\xi}^{\alpha}$ are a nodal displaceemnt and a basis function of of the α-th node. Since the unknown funcdtion is $\boldsymbol{u}^{\alpha}$'s, substituting this $\boldsymbol{u}$ into a continuum Lagraginan results in a functional for $\boldsymbol{u}^{\alpha}$'s, i.e., $\mathcal{L} = \int_V \ell(\boldsymbol{v}^{\alpha}, \boldsymbol{u})\,\mathrm{d}v$ with $\boldsymbol{v}^{\alpha} = \dot{\boldsymbol{u}}^{\alpha}$. Again, the Legendre transform of $\boldsymbol{p}^{\alpha} = \frac{\partial \mathcal{L}}{\partial \boldsymbol{v}^{\alpha}}$ converts $\mathcal{L}$ to a Hamiltonain for $\boldsymbol{p}^{\alpha}$ and $\boldsymbol{u}^{\alpha}$,

$$\mathcal{H}[\boldsymbol{p}^{\alpha}, \boldsymbol{u}^{\alpha}] = \sum_{\alpha} \boldsymbol{v}^{\alpha}\cdot\boldsymbol{p}^{\alpha} - \mathcal{L}[\boldsymbol{v}^{\alpha}, \boldsymbol{u}^{\alpha}],$$

where [] is used for $\mathcal{L}$ or $\mathcal{H}$ to emphasize that it is a functional. The cannonical equations are

$$\dot{\boldsymbol{p}}^{\alpha} = -\frac{\partial \mathcal{H}}{\partial \boldsymbol{u}^{\alpha}} \quad \text{and} \quad \dot{\boldsymbol{u}}^{\alpha} = \frac{\partial \mathcal{H}}{\partial \boldsymbol{p}^{\alpha}}.$$

References

[1] Aagaard, B. T., Anderson, G. and Hudnut, K. W. [2004], Dynamic rupture modeling of the transition from thrust to strike slip motion in the 2002 Denali Fault Earthquake, Alaska, *Bull. Seism. Soc.Am.*, **94**(6B), S190–S201.

[2] Andrews, D. J. [1976], Rupture velocity of plane strain shear cracks, *J. Geophys. Resear.*, **81**, 5679–5687.

[3] Ishimura, D., Okada, S., Niwa, Y. and Toda, S. [2015], The surface rupture of the 22 November 2014 Nagano-ken-hokubu earthquake (Mw 6.2), along the Kamishiro fault, Japan, *Active Fault Resear.*, **43**, 95–108 (in Japanese).

[4] Dalguer, L., Irikura, K. and Wu, H. [2017], Permanent displacement from surface-rupturing earthquakes: insights from dynamic rupture of Mw7.6 1999 Chi-chi Earthquake, *Proc. of the 16th World Conference on Earthquake Engineering*, Santiago, Chile, paper-1004.

[5] Dietrich, J. H. [2007], Applications of rate- and state-dependent friction to models of fault slip and earthquake occurrence, in *Treatize on Geophysics* (ed. Kanamori, H.), Vol. 4, Chap. 4,, 107–129.

[6] FrontISTR Formum [2017], *FrontISTR ver.4.5*, http://www.multi.k.u-tokyo.ac.jp/FrontISTR/files/FISTRv4.5E.pdf, retrieved 10 January 2018.

[7] Geller, R. J. [1976], Scaling relations for earthquake source parameters and magnitudes, *Bull. Seism. Soc. Am.*, **66**, 1501–1523.

[8] Goodman, R. E., Taylor, R. L. and Brekke, T. L. [1968], A model for the mechanics of jointed rocks, *Journal of A.S.C.E.*, **94**(SM3), 637–659.

[9] Hairer, E., Lubich, C. and Wanner, G. [2006], *Geometric Numerical Integration: Structure-Preserving Algorithms for Ordinary Differential Equations*, Springer, New York.

[10] Harris, R. and Day, S. [2008], Dynamics of fault interaction: parallel strike-slip faults, *J. Geophys. Resear.*, **98**, 4461–4472.

[11] On-site Fault Assessment Method Review Committee of Japan Nuclear Safety Institute (JANSI) [2013], *Assessment Methods for Nuclear Power Plant against Fault Displacement*, JANSI-FDE-03, Japan.

[12] Kame, N., Rice, J. R. and Dmowska, R. [2003], Effects of prestress state and rupture velocity on dynamic fault branching, *J. Geophys, Resear.*, **108**(B5), doi:10.1029/2002JB002189.

[13] Kase, Y. and Kuge, K. [2001], Rupture propagation beyond fault discontinuities; significance of fault strike and location, *Geophys. J. Int.*, **147**, 330–342.

[14] Okada, Y. [1985], Surface deformation due to shear and tensile faults in a half-space, *Bull. Seism. Soc. Am.*, **75**(4), 1135–1154.

[15] Rieben, R., White, D. and Rodrigue, G. [2004], High-order symplectic integration methods for finite element solutions to time dependent Maxwell equations, *IEEE Trans. Anthennas and Propagation*, **52**, 2190–2195.

[16] Ruth, R. D. [1983], A canonical integration technique, *Nuclear Science, IEEE Trans. on NS-30*(4), 2669–2671.

[17] Sawada, M., Haba, K. and Hori, M. [2016], Computational study on a numerical method for fault-displacement estimation, *Journal of JSCE*, **72**(2), I_676–I_685 (in Japanese).

[18] Sawada, M., Haba, K. and Hori, M. [2017], High performance computing for fault displacement simulation, *Journal of JSCE*, **73**(2), in print (in Japanese).

[19] Vosbeeka, P. W. and Mattheija, R. M. M. [1997], Contour dynamics with symplectic time integration, *Journal of Computational Physics*, **133**, 222–234.